Contents lists available at ScienceDirect

Composites Science and Technology

journal homepage: www.elsevier.com/locate/compscitech

Boron nitride-reinforced porous aramid composites with enhanced mechanical performance and thermal conductivity

Andrea Rubio-Aguinaga [a], José Antonio Reglero-Ruiz [a], Alejandra García-Gómez [b],
Elisa Peña Martín [b], Shinji Ando [c], Asunción Muñoz [a], José Miguel García [a],
Miriam Trigo-López [a,*]

[a] *Departamento de Química, Facultad de Ciencias, Universidad de Burgos, Plaza de Misael Bañuelos s/n, 09001, Burgos, Spain*
[b] *Gnanomat S.L, Campus Cantoblanco, Madrid Science Park, Calle Faraday, 7, 28049, Madrid, Spain*
[c] *Department of Chemical Science and Engineering, Tokyo Institute of Technology, Ookayama 2-12-1-E4-5, Meguro-ku, Tokyo, 152-8552, Japan*

ARTICLE INFO

ABSTRACT

Aramids are materials with high-performance properties and used in advanced applications, including bullet-proof vests and aerospace industry components. Consequently, research is focused on improving their properties and reducing their density to achieve fuel reduction and enhanced comfort. Herein we describe the preparation of dense, micro, and nanoporous aramid films containing hexagonal boron nitride (hBN) with two objectives: improving mechanical performance and increasing thermal conductivity (TC) in porous films for specific applications. The preparation procedure is simple and scalable, involving the addition of hBN and a porosity promoter to control the porous structure in the film's casting solution. Tensile tests revealed that the inclusion of 10% of hBN in microporous aramids led to a 130% increase in Young's modulus and 63% reduction in material's density compared to the dense commercial aramid. The orientation of the hBN in the films was also evaluated by considering the XRD and the thermal properties of the films. The films containing hBN exhibited enhanced TC and thermal diffusivity (TD) together with a very low density and improved mechanical performance, which can benefit applications in the aerospace industry, protective equipment, and battery separators.

1. Introduction

Aromatic polyamides or aramids are advanced high-performance materials with outstanding mechanical and thermal properties. Additionally, they exhibit low density and are electrical and thermal insulators. They can be manufactured in various forms, including fibers, textiles, films, or composites. Their remarkable properties make them ideal materials for a wide range of applications including protective clothing, antiballistic apparel, electrical insulators, tire reinforcement, asbestos replacement, and components in boats, aircraft, cars, or sports equipment [1]. Current research on aramids is focused on three main aspects. Firstly, there is a focus on reducing their density while preserving their properties to reduce fuel consumption in transportation applications, enhance comfort in protective equipment, or obtain porous materials for batteries [2–5]. Second, efforts are being made to expand their applications by incorporating new monomers into the aramid's structure and leveraging their high-performance properties [1,6–9].

Finally, there is a goal to improve their transformability and/or enhance their thermal and mechanical performance by introducing new monomers or reinforcing them with other materials such as carbon nanomaterials and ceramics [10–13].

In our previous works, we developed a straightforward methodology to prepare porous aramid films using a casting procedure. Ionic liquids or inexpensive polymers (polyvinyl alcohol, cellulose acetate, or poly(2-ethyl-2-oxazoline)) were used as porosity promoters (PPs) in the film casting procedure [3,14]. The elimination of these PPs after film formation rendered porous materials with very low density while maintaining or improving their outstanding mechanical performance. Later, we also reinforced porous aramid films with functionalized carbon nanomaterials, improving their thermal and mechanical properties [10]. In a step forward, to further enhance their properties, we decided to explore the reinforcement of these porous, low-density aramids with inorganic materials possessing anisotropic shapes, specifically with hexagonal boron nitride (hBN), as it has not been previously addressed.

Since the discovery of graphene, various 2D materials have gained attention as promising candidates for many applications. hBN is one of them since it serves as a structural counterpart of graphite, offering high stability and exceptional mechanical strength. In fact, it is considered a more desirable candidate than graphene as mechanical reinforcing material [15]. Additionally, hBN is an excellent electrical insulator while possessing high thermal conductivity and low friction coefficient [16]. These advantageous properties have led to its utilization in various fields, including energy storage applications, supercapacitors, batteries, photonics, electronic devices, composites for thermal applications, composite materials with improved corrosion, chemical and mechanical resistance, catalytic applications, biomedical applications, etc. [17,18].

Commercial aramids, poly(*m*-phenylene isophthalamide) and poly (*p*-phenylene terephthalamide) are high-performance insulating materials. As a result, they have been widely used in electrical equipment such as traction motors, generators, transformers, etc. However, the increasing demand for large capacities, high voltages, high power densities, and compact sizes necessitates the improvement of thermal conductivity in these materials [19]. In this regard, aramids face limitations due to their low thermal conductivity, which hinders heat dissipation, leads to heat accumulation, and negatively impacts operational efficiency and service life. Consequently, numerous researchers have directed their efforts to prepare aramid composites containing hBN. The objective is to design materials with exceptional performance and enhanced thermal conductivity, while also maintaining excellent electrical insulation properties. This approach aims to extend the service life of these materials and broaden their applications in the electronic industry by mitigating the risk of overheating. Many examples in the literature use aramid nanofibers for this purpose [20–23].

Current research reveals the potential to develop porous polymer foams composites with thermally conductive fillers as lightweight thermal management materials. This may seem counter-intuitive since porous materials are commonly used for thermal insulation, but reducing the weight of materials is crucial for energy saving nowadays. Furthermore, foaming can help reduce material consumption, leading to more environmentally sustainable systems [24]. In this regard, various strategies have been pursued for the preparation of porous composites with hBN, as reported in the literature. For instance, high-density polyethylene/hBN composites were obtained through supercritical fluid foaming in an injection molding process [25]. However, this technique is expensive and produces *in situ* exfoliation. Moreover, it is not viable for large production. Similar issues arise with other foaming techniques, such as the freeze-casting method for preparing epoxy/hBN porous composites or using Ni foams as templates to prepare polydimethylsiloxane composite foams [26,27]. Phase inversion processes have also been explored to produce porous composites of poly(vinylidene fluoride) with hBN, but they tend to yield materials with irregular porosity [28]. Other reported strategies include high-internal-Pickering emulsification and hot pressing for preparing polyimide/BN porous composites, as well as melt compounding and salt leaching for lightweight polyethylene/hBN composites [29,30]. In general, the described procedures for preparing porous composites with hBN are expensive, tedious, or not easily scalable. Moreover, no literature on preparing porous aramid/hBN composites was found.

For these reasons, this work aims to provide a straightforward, scalable, and effective strategy to develop dense and porous aramid composite films containing hBN with high strength, toughness, and improved thermal conductivity. The development of these materials enables their use in advanced applications such as battery separators, where porous materials with good heat dissipation capability are needed [31]. Additionally, improving mechanical performance and heat dissipation, along with reducing the density of aramids, is a crucial issue for applications related to the aerospace industry to reduce fuel consumption. This can also benefit other areas, such as the development of bulletproof vests. By improving their mechanical performance, aramids can offer superior protection while providing increased comfort by reducing weight and improving heat dissipation, which reduces sweating during wear.

2. Materials and methods

2.1. Materials

All materials used in this work are commercially available and were used as received: *N,N*-dimethylacetamide (DMA, Sigma-Aldrich, >99%), LiCl (Sigma-Aldrich, ≥99%), polyvinyl alcohol (PVA) (Applichem, 85–89% wt., 10–26 KDa), poly(2-ethyl-2-oxazoline) (PEOx) (ThermoFisher, 50 KDa). Meta-aramid fiber ARAWIN® (PA) (Nonwoven regular staple fiber of average length 6.4 mm), was supplied by Toray Advanced Materials Inc. (Korea). Hexagonal boron nitride (hBN) nanoplatelet powder (Hexotene®) with lateral dimensions up to 5 μm was obtained from Versarien.

2.2. Methods

Scanning Electron Microscopy (SEM) micrographs were obtained using a JEOL JSM-6460LV Scanning Electronic Microscope. The samples were cut after liquid nitrogen freezing and coated with gold. To characterize the cellular structure of the film samples in terms of the average bubble radius $\overline{R}$ and average cell density, ImageJ® software was used, counting the number of cells (n_i) in each SEM micrograph and their radius (R_i), using Equation (1):

$$\overline{R} = \frac{\sum_{i=1}^{N} n_i R_i}{\sum_{i=1}^{N} n_i} \tag{1}$$

The density of dense films (ρ) was calculated using the dimensions and weight of the samples. The width of the films was measured five times using a digital micrometer (Sonline 25 mm/0.001 mm), and the results were averaged. The density of the porous film (ρ_p) was estimated from SEM images using ImageJ®, according to Equations (2) and (3), where V_f is the gas fraction per volume and $\overline{d}$ is the average diameter of the pore.

$$V_f = \frac{\pi \overline{d}^3 N_c}{6} \tag{2}$$

$$\rho_p = (1 - V_f)\rho_d \tag{3}$$

Atomic Force Microscopy (AFM) images of the film's samples were acquired using an Alpha300R – Alpha300A model from WITec. They were obtained at 25 °C, and using the tapping mode and a 42 N/m tip.

The thermogravimetric analysis (TGA) was performed using both synthetic air and nitrogen atmospheres using a Q50 TGA from TA Instruments. First, the samples (around 5 mg) were heated to 100 °C and kept at that temperature for 10 min to remove the moisture content. Then, they were heated to 800 °C at 10 °C/min to perform the analysis.

Differential Scanning Calorimetry (DSC) measurements were performed using a Q200 TA DSC from TA Instruments and 20 mg samples. First, the sample was heated at 15 °C/min from room temperature to 150 °C, and kept at that temperature for 30 min to remove the humidity and possible solvent traces content. Next, the sample is cooled to 30 °C at 20 °C/min and heated to 300 °C at 15 °C/min to analyze the thermal transitions.

The mechanical performance of the films was evaluated using 5 × 40 mm strips cut from aramid films and oven dried (80 °C, 24 h). A SHIMADZU EZ Test Compact Table-Top Universal Tester and mechanical clamps were used to perform the tensile tests. The tests were performed at an extension rate of 5 mm/min, using at least five strips of each sample and averaging the results.

Wide angle X-ray diffraction (XRD) was used to characterize the

composite films. An X-ray Bruker D8 Discover diffractometer was used, with a type KFL Cu (λ = 1,54 Å) radiation and a Lynx-Eye XE detector.

Specific heat measurements were performed using a DSC30 Mettler Toledo Instrument, following the UNE EN ISO 11357–3, 2013 standard. Three samples of each film (films of 20 mg) were tested, and the results were then averaged.

Thermal conductivity (TC) measurements were performed using the Transient Plane Source (TPS) method [32], which allows for fast and accurate determinations of TC values and is widely used in micro and nanocellular polymeric materials [33]. A HOT-DISK TPS 2500 S equipment with a 7.854 mm radius sensor was employed. The sensor is heated using a transient pulse, and its resistivity variation is related to the material's TC. The measurements were performed on 4 cm diameter film discs, with a measuring time of 20 s, and a 0.5 W heating power. Three replicates of each film measurement were taken, and the results were averaged. The isotropic thermal diffusivity (TD) was calculated from the TC, the density of the films, and heat capacity.

Measurements of TD along the out-of-plane thickness direction ($a_\perp$) were performed at room temperature using 10-37 μm-thick aramid films cut in 50 × 5 mm strips. These films were thinner than the ones used for the other techniques (thicknesses ranging from 50 to 140 μm). The films were coated with a carbon layer, and $a_\perp$ values were measured with a temperature wave analyzer (TWA, ai-Phase mobile 1u, Tokyo, Japan) using the propagation of temperature waves penetrating the films [34], with an applied voltage of 1.8 V. Prior to the measurements, $a_\perp$ value was calibrated using standard polyimide films (Kapton, UPILEX x 2). Each sample was measured with two different films. Seven different TD values were obtained at different points of the film, excluding the largest and smallest values, and averaging the rest of the results.

2.3. Preparation of dense and porous films

The aramid films were prepared by following the standard solution casting method. Firstly, a mixture of solvent (DMA, 5 mL) and solubility promoter (LiCl, 0.10 g) was heated to 80 °C. Then, commercial poly (*m*-phenylene isophthalamide, MPIA, 0.35 g) was added to the mixture and stirred until completely dissolved. We will refer to the mixture DMA/LiCl/MPIA as the 'casting solution'. To prepare the films, the casting solution was poured onto a glass plate and kept inside an air-circulating oven at 80 °C for 24 h to remove the solvent. To obtain microporous (μP-) or nanoporous (nP-) aramid films, PVA (10 % wt. respect to the aramid) or PEOx (100 % wt. respect to the aramid), respectively, was added to the casting solution along with the PPs. The mixture was stirred for at least 1 h, as reported previously [2]. To prepare the films containing hBN, the corresponding amount of hBN particles (10 wt% or 20 wt% in the aramid composites) was added to the casting solution and stirred for an additional 1 h before pouring it onto the glass plate.

The porous structure in the films containing PPs was generated by removing the PPs in water after the film formation. The films were then immersed in hot water (80 °C) for 8 h, changing the water at least four times. The detailed procedure was described elsewhere [2].

3. Results and discussion

3.1. Preparation of films

In our previous works, studies regarding the influence of the amount and nature of PPs in the development of aramids with the cellular structures were carried out, evaluating their thermal and mechanical performance compared to dense *m*-aramid films (see Refs. [2,3,14]). In the last one, we studied the influence of PVA and PEOx as PPs. The obtention of the porous aramid films involved the addition of a PP in the casting solution. A film is formed after the evaporation of the solvent, and the porous structure is obtained after removing the PP in water. When a 10 % wt. of PVA to the *m*-aramid is used as the PP, a very homogenous and opened-cell microporous structure (microporous films,

μP-) is obtained. Porosity can be observed both on the surface and in the cross-section of the films, with pore sizes of 2 μm of radius and a 68% density reduction compared to a dense aramid. On the other hand, when 100% PEOx to the aramid is used as PPs, opened-cell nP-films, structured polymers are obtained, with pore size radius between 0.1 and 0.02 μm and 43% density reduction with respect to the MPIA film.

In this work, we fabricated different aramid-hBN porous and dense composites by adding hBN in the cast solution (Fig. 1 and Table 1), as mentioned in Section 3.2. We also included a dense MPIA film and μP- and nP-films without hBN for comparison. Then we tested their properties to evaluate the influence of hBN in the aramid films, taking advantage of our previous work. The dense MPIA film was transparent, while the micro and nP-films were opaque due to their porosity, which caused light scattering. Films containing hBN prepared by our procedure were macroscopically homogeneous (see the pictures of the films in Fig. S1 in the electronic Supplementary Information, SI). The white color intensified with increasing amounts of hBN.

3.2. Pore sizes and distribution of hBN

The surface and cross-section of the films were analyzed using SEM to evaluate the dense and porous structure and the distribution of hBN nanoplatelets within the films.

Films prepared without PPs exhibit a dense structure with a homogeneous distribution of hBN platelets along the cross-section, as shown in Fig. 2 a), b), and c). These are cross-sectional SEM micrographs of the entire width of the films (x1,000 magnification) with varying proportions of hBN. Upon closer inspection of the films (x3,000 magnification, Fig. 2 d) e) and f)), hBN platelets are clearly visible, revealing a better distribution of the hBN in the 10% hBN film. The μP-films prepared using PVA or the nP-film using PEOx as PP maintain the original porous structure after adding hBN. Fig. 2 g)-r) displays the cross-sectional SEM micrographs of the entire width of μP-MPIA and nP-MPIA films, with scale bars provided. In both porous morphologies, the distribution of hBN remains homogenous along the films when using 10% hBN, but tends to form aggregates [31] and accumulate at the bottom of the film during the casting procedure when using 20% hBN, primarily due by gravity. In our easy and cost-effective casting procedure for film preparation, there is limited opportunity for the orientation or the hBN platelets beyond their natural alignment due to their two-dimensional structure. As a result of their high aspect ratio, they tend to align horizontally within the film [35], especially in nP- films, as later demonstrated by XRD in this study.

Additionally, the μP-films exhibit dispersed surface porosity, and when these films are loaded with hBN, the surface porosity becomes more isolated and irregular (see Figs. S2 and SI). In contrast, no surface porosity is observed in nP-films. Moreover, hBN platelets can be observed reaching the surface of the films when using 20 wt% of hBN in the film formulation.

The pore sizes and distributions of the prepared films, as well as their density reduction compared to an MPIA film, are summarized in Table 2. The dense MPIA films containing hBN (MPIA-10hBN and MPIA-20hBN) show slight reductions in density compared to the pristine film without hBN. The μP-films exhibit the largest density reduction, up to 68% compared to MPIA. However, this density reduction is less pronounced in the film containing 20 wt% of hBN (μP-MPIA-20hBN), likely due to the aggregation of hBN platelets on one of the film's surfaces, which interferes with porosity formation. The reduction in film density depends on the amount and type of PP, rather than the presence of hBN, as observed in the nP-films. In terms of cellular structure, the presence of hBN in μP-films has a minimal influence on pore sizes. However, in nanoporous morphologies, the influence is more apparent, resulting in larger pore sizes.

The surface of the films was also analyzed using AFM to detect the presence of hBN laminates. Fig. 3 a) shows the surface topography of the different porous films containing hBN, with dispersed porosity observed
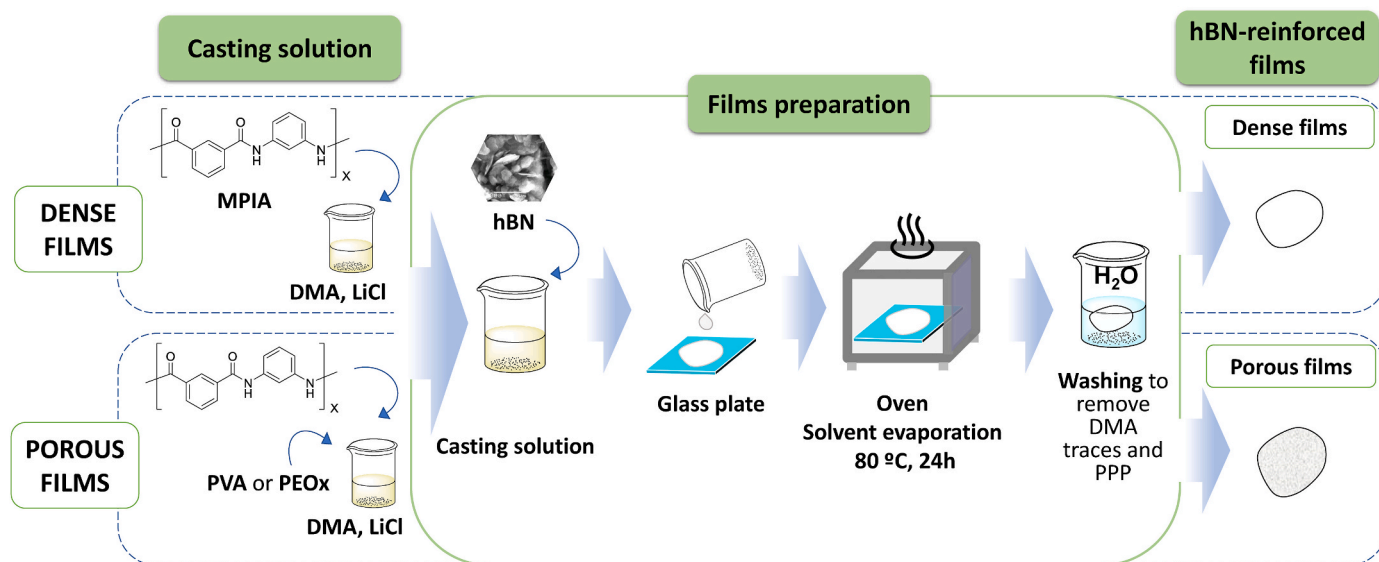
Fig. 1. Preparation of dense and porous hBN-reinforced aramid films.

Table 1
Nomenclature, materials, and quantities used to prepare the composite films.

Film[a]	Porosity promoter (wt. %)	Porosity promoter (mg)	hBN (wt. %)	hBN (mg)	Dense/porous
MPIA			–	–	Dense
MPIA-10hBN			10	35	
MPIA-20hBN	–		20	70	
µP-MPIA	PVA (10)	35	–	–	Microporous
µP-MPIA-10hBN	PVA (10)	35	10	35	(µP-)
µP-MPIA-20hBN	PVA (10)	35	20	70	
nP-MPIA	PEOx (100)	350	–	–	Nanoporous
nP-MPIA-10hBN	PEOx (100)	350	10	35	(nP-)
nP-MPIA-20hBN	PEOx (100)	350	20	70	

 [a] All of the solutions used to prepare the films also contain DMA (5 mL), commercial *m*-aramid (PA) (350 mg) and LiCl (100 mg).

for µP-films, along with hBN laminates in the film containing 20% wt. of hBN. Moreover, the amplification of the 3D images of these films (Fig. 3 b)) provide a closer view of the presence of hBN laminates reaching the surface in the films containing 20% hBN.

3.3. X-ray diffraction (XRD)

XRD analysis provides more accurate information about the orientation of hBN platelets in the composites compared to SEM images. hBN is a crystalline solid, and XRD characterization allows for the unequivocal confirmation of the presence and integrity of hBN after the washing procedure at 80 °C. Initially, the hBN was characterized (PDF-00-034-0421, a = b = 2, Å, c = 6,6562 Å) together with MPIA film. Fig. S3 displays the XRD profiles of the films, where the amorphous peak of aramid (between 18° and 25°) and the crystalline peaks of hBN (26,74°, 41,62°, 49,68°, and 54,94°) can be observed, confirming the presence and integrity of hBN. These XRD patterns can be attributed to the (002), (100), (004), and (103) planes of the crystal of the hexagonal structure

of the hBN [36]. The (002) peak corresponds to horizontally oriented hBN, while the (100) peak corresponds to vertically oriented hBN [37, 38] (Fig. 4 a)).

By plotting the intensity of these peaks for each film (Fig. 4 b)), the XRD patterns can provide additional information about the alignment of hBN within the films. To illustrate this, we calculated the ratio (δ) of the (002) to the (100) peak intensity, using Equation (4) [39]:

$$\delta(\%) = \frac{I_{(100)}}{I_{(100)} + I_{(002)}} \times 100 \qquad (4)$$

The XRD analysis reveals that the intensity of the (002) peak slightly increases with the increasing amount of hBN in dense films. The increase in both horizontally and vertically oriented hBN in dense films can be attributed to the response of more hBN layers to X-ray. However, a different trend is observed in µP-films, where higher hBN loading decreases the horizontally oriented hBN and increases the ratio of vertically oriented hBN. This is consistent with our fabrication procedure, where hBN platelets are primarily oriented due to gravity during the casting process. With higher hBN content, the increased viscosity of the mixture impairs hBN alignment and causes aggregation phenomena, as observed in the SEM micrographs [40]. Furthermore, in porous films, the orientation of the hBN platelets is influenced by the nature of the PP. During the process of pore formation, phase separation occurs during film casting, followed by the removal of the PP. In the films, larger PVA phases are formed compared to PEOx, resulting in the formation of larger pores that are typically within the size range of hBN platelets once the PPs are removed. Considering the stronger interactions between MPIA and hBN compared to PVA, the hBN platelets tend to preferentially locate themselves in the MPIA regions [41,42]. This preferential localization leads to the platelet orientation, resulting in higher proportion of vertically oriented hBN (located in the pore walls), which is primarily observed in the SEM micrograph. On the other hand, when PEOx is used as the PP, very small pores are formed, and the hBN platelets are positioned across the polymer phases, orienting themselves in-plane.

3.4. Thermal analysis

The TGA curves of the prepared films were measured to analyze the thermal degradation of the films containing hBN, compare them with the pristine films, and verify the presence and amount of hBN after washing the films. The thermal degradation of the dense films (Fig. 5)
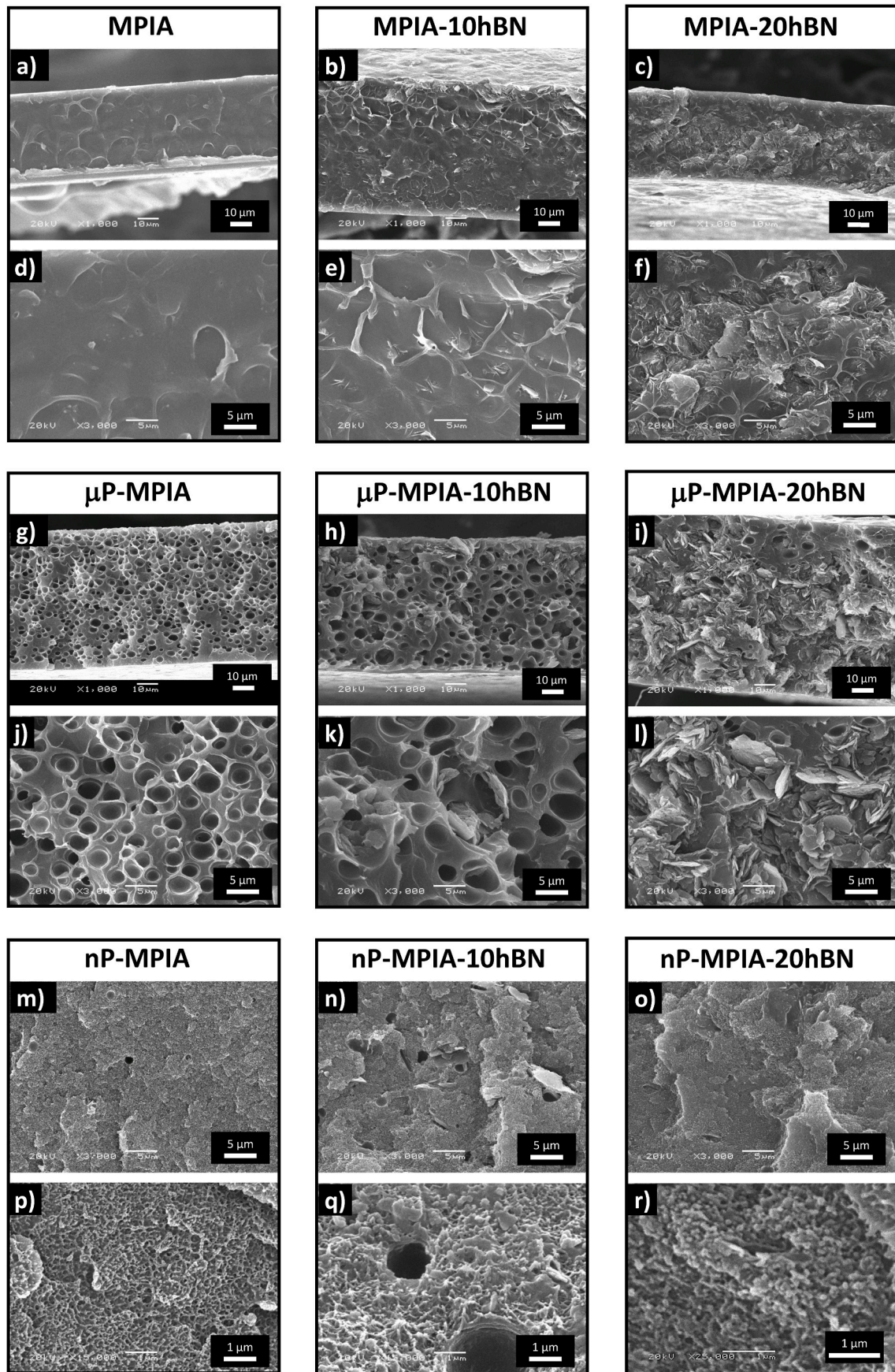
Fig. 2. SEM micrographs of the cross-section of dense, micro- and nanoporous MPIA films.

Table 2
Pore sizes, distribution, and density of the films.

Film	Cross-section porosity	Pore size $\overline{R}$ (μm)	Surface porosity	Pore size $\overline{R}$ (μm)	Density (g/cm³)	Density reduction (%)
MPIA	–		–		1.27	–
MPIA-10hBN	–		–		1.29	4
MPIA-20hBN	–		–		1.11	5
μP-MPIA	Homogeneous	2	Homogeneous	2.5	0.45	68
μP-MPIA-10hBN	Homogeneous	3.1	Disperse		0.53	63
μP-MPIA-20hBN	Homogeneous[a]	2.7	Disperse		0.84	41
nP-MPIA	Homogeneous	0.02–0.1	No		0.81	43
nP-MPIA-10hBN	Homogeneous	0.05–0.14	No		0.86	39
nP-MPIA-20hBN	Homogeneous	0.05–0.15	No		0.87	39

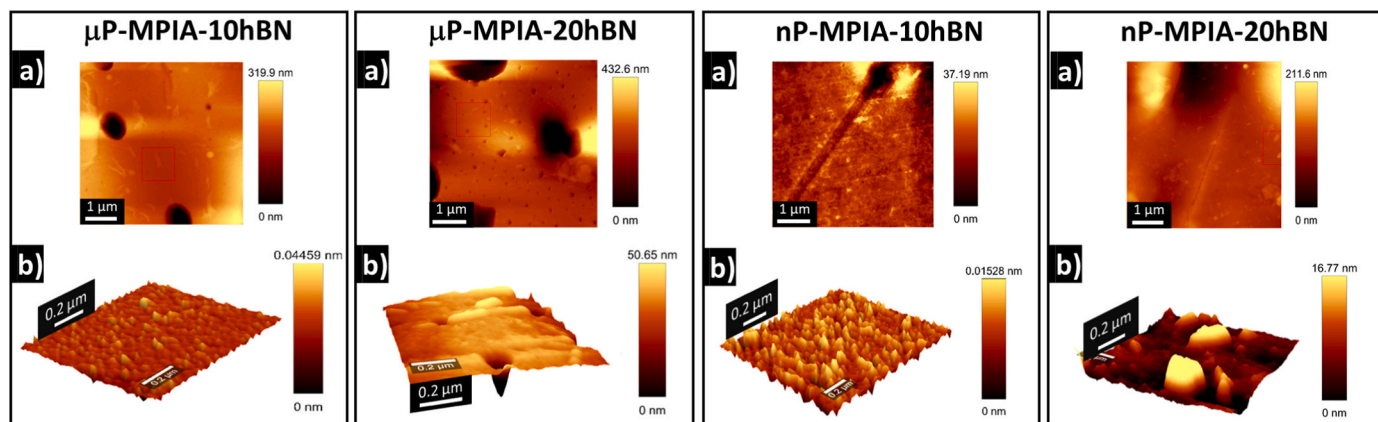[a] Homogeneous in the regions without hBN accumulation.

Fig. 3. Surface AFM topography of a) the micro and nanoporous films containing hBN, and b) their amplification.
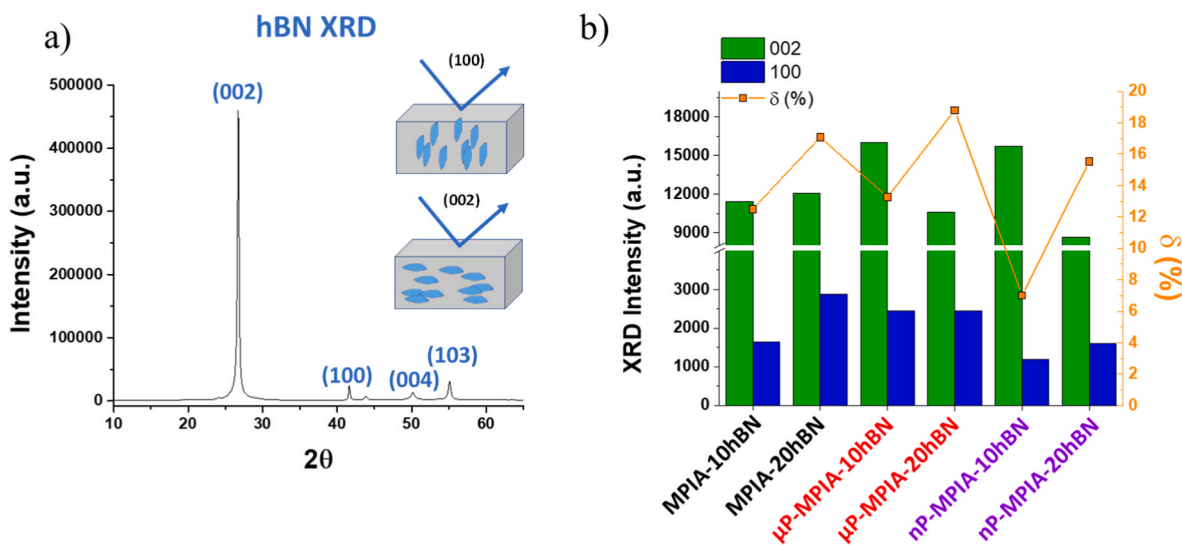

Fig. 4. a) Illustration of the orientation of hBN on the XRD pattern. b) Intensity variation of the (002) and (100) peaks of hBN in each film.

demonstrates the positive effect of hBN presence in the films on the thermal performance, as it increases the degradation temperature and reduces weight loss at high temperatures compared to the pristine films. This effect is also observed in the micro- and nP-films (refer to Fig. S4). Table S1 provides a summary of the thermal degradation performance of the films, including the temperatures at which 5% and 10% weight loss occur (T_5 and T_{10}), char yield, and limiting oxygen index (LOI). The presence of hBN increases all these parameters in dense films. However, in micro and nP-films, T_5 and T_{10} values are slightly lower than those in the dense films, possibly due to the presence of PVA and PEOx residues

[2]. The char yield of the films under a synthetic air atmosphere aligns with the hBN loading percentage, and under a nitrogen atmosphere, it increases as the hBN content increases, as expected. This results in a noticeable increase in the LOI values. DSC results of the dense films containing hBN show no variation in the Tg values (see Fig. S4).

3.5. Mechanical performance

The mechanical performance of the pristine films and hBN composite films was evaluated in terms of their relative values (E_r, relative Young's
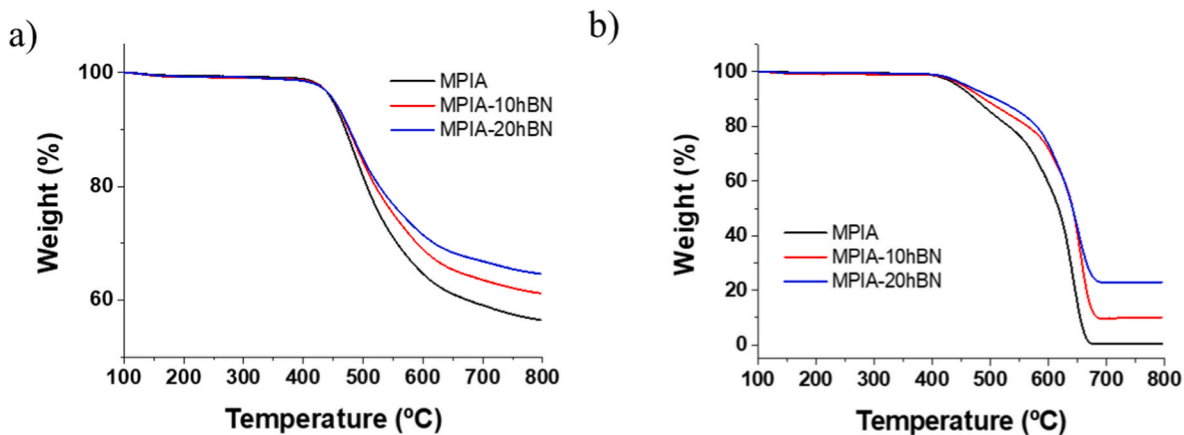
Fig. 5. Thermograms of the dense films in a) nitrogen atmosphere and b) in synthetic air atmosphere.

moduli, σ_r^{bp} relative tensile strength, and ε_r relative elongation at break). These relative values were obtained by averaging the mechanical parameters of the films and dividing them by each film's density, allowing for a comparison with the properties the dense materials (Fig. 6 and Table S1).

Remarkable improvements in the performance of dense materials containing 10% of hBN were observed, resulting in a 60% increase in the relative Young's modulus and a 20% increase in tensile strength. However, when higher amounts of hBN were loaded into the composite material, these properties were significantly worsened due to poor dispersion within the matrix. Adequate dispersion is crucial for achieving effective load transfer and an actual performance improvement. The μP-films without hBN (μP-MPIA) also exhibited improved mechanical performance compared to the corresponding dense material [2]. The addition of 10% hBN in the film formulation of μP-films (μP-MPIA-10hBN) resulted in a 48% increase in Young's modulus compared to μP-film (μP-MPIA) and a 131% increase compared to the dense material (MPIA) without hBN. These observations are clearly depicted in Fig. S5, which illustrates the stress-strain curves in terms of relative stress (σ_r) as a function of unitary deformation (ε). However, adding larger amounts of hBN led to a decrease in mechanical performance in terms of Young's modulus and tensile strength. Additionally, the tensile strength of μP-MPIA-10hBN film increased by 128% compared to the dense, unreinforced material.
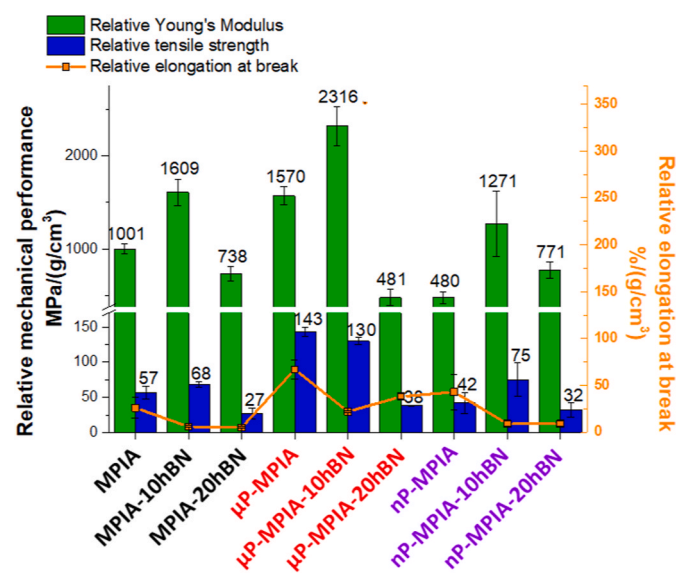
The reinforcement of the nP-films also enhances their mechanical performance; however, it is not as significant as in the μP-films. It should be noted that adding 20% hBN in the composite formulation worsens the mechanical performance in all cases due to poor dispersion. As anticipated, the presence of hBN in the composite formulation leads to a reduction in elongation at break. When comparing the different composites containing 10% hBN (Figure S5 b), the most notable mechanical reinforcement is clearly observed in the μP- composite.

3.6. Thermal conductivity and diffusivity

Then, we aimed to evaluate the influence of porosity (from nanometric to micrometric scale) and the quantity of hBN (10 and 20 wt%) on the thermal conductivity (TC) of aramid films. show The TC values (λ) obtained in our films are presented in Table S2 and Fig. 7a). It can be observed that the λ values of the pristine films without hBN range from 0.13 W/m·K in the neat nanocellular aramid nP-MPIA (with smaller pore size) to 0.67 W/m·K in dense aramid containing 20% of hBN (MPIA-20hBN). The influence of porosity is evident, where the TC decreases as the pore size decreases, in accordance with the Knudsen effect, which reduces the contribution of the gaseous phase to the TC [43,44] (see also Fig. 7f)). This is demonstrated by comparing the TC of μP-films without hBN (μP-MPIA, 0.21 W/mK) to that of nP-film without hBN (0.13 W/m·K). The significant influence of hBN% in the TC is also evident, with a 160% increase in dense films with 20% hBN compared to dense MPIA, a 42% increase in μP-films, and an 83% increase in nP-films (Fig. 7c)). In general, lower the density results in lower TC. However, when TC is correlated with film density (Fig. 7e)), the Knudsen effect comes into play. When comparing the two porous films with 20% hBN, μP-MPIA-20hBN and nP-MPIA-20hBN, a lower conductivity is observed in the latter, aligning with the smaller pore sizes at similar densities.

Thermal diffusivity, TD, which measures the velocity of heat propagation through thermal conduction, was calculated by dividing the TC by the heat capacity and density of the films. As expected, there is a direct correlation with the TC. Fig. 7b) shows that TD increases with an increase in hBN% for the dense and nP-films. However, in the μP-films, a film containing 20% hBN (μP-MPIA-20hBN) results in a decrease in TD. This property is related to the density of the materials, and the μP-films with 20% of hBN exhibit higher density compared to the other μP-films, which explains the lack of direct correlation between the TC and TD. The increment in both properties is very similar for the dense and μP-films compared to the material without hBN (Fig. 7c)). Furthermore, the out-of-plane TD ($a_\perp$) of the films was also measured and found to increase with the hBN content in the film. However, it was not possible to measure the in-plane TD because the films were very thin, and creases were formed during the removal of PPs to obtain porous films, leading to unreliable results. Nevertheless, based on the estimated TD from the TC
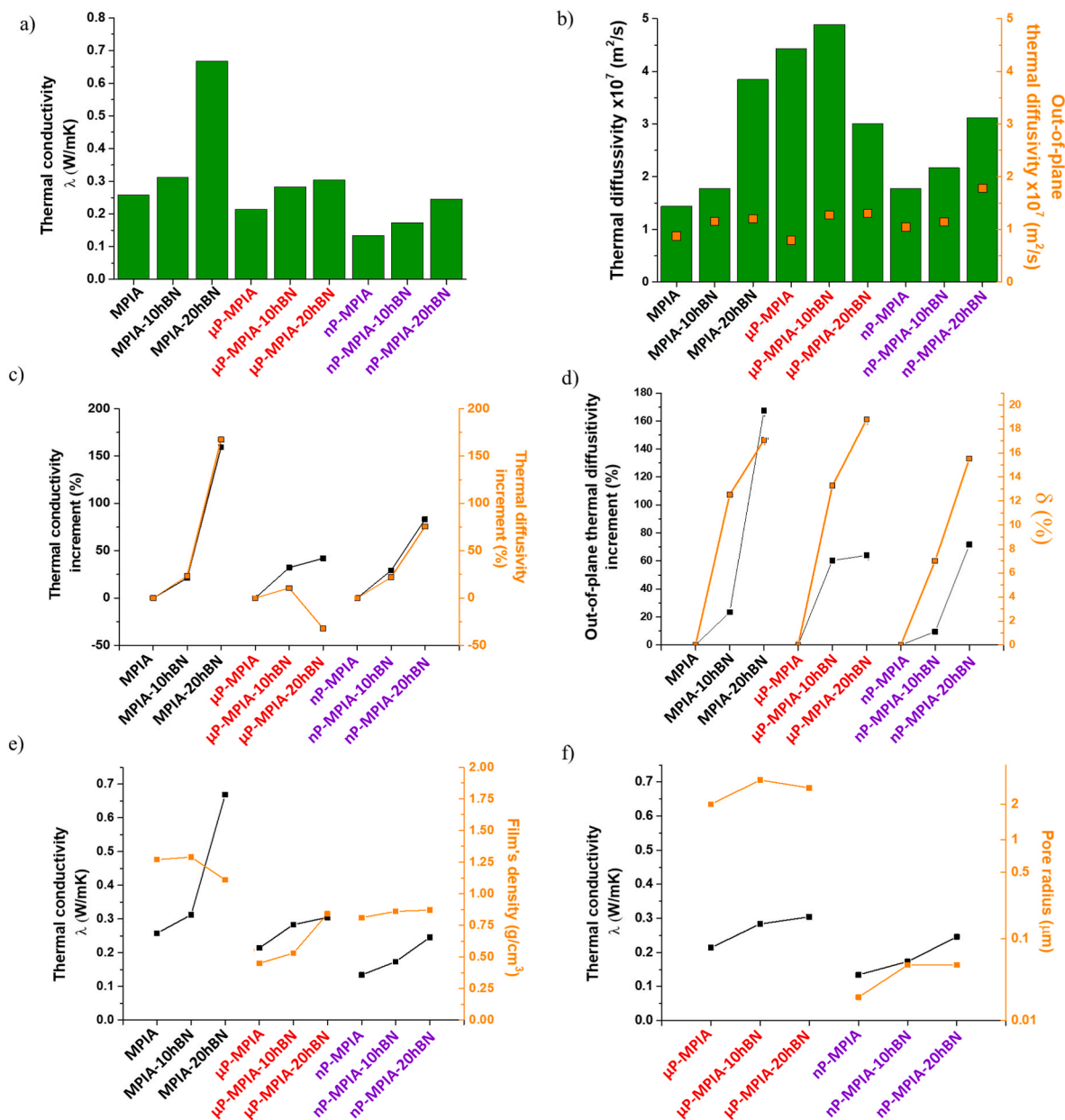

Fig. 6. Mechanical performance of the dense and porous films containing hBN.

Fig. 7. a) Thermal conductivity (TC) of the dense and porous films with different amounts of hBN, b) thermal diffusivity (TD) (x10^6) and out-of-plane thermal diffusivity (x10^7, $a_\perp$) of the films prepared, c) increment of TC and TD of the films compared to the dense and porous unreinforced films, d) relationship between the $a_\perp$ and the ratio of vertically oriented to the horizontally oriented hBN (δ), e) relationship between the TC of the films and their density, and f) relationship between the TC and the pore radius of micro and nanoporous films.

measurements, it is suggested that the in-plane TD values should be slightly higher than $a_\perp$ due to the natural tendency of hBN platelets to align horizontally, as confirmed by XRD. The increase in $a_\perp$ compared to the pristine films was correlated with the degree of hBN orientation in the films (Fig. 7d)), which was estimated from the ratio (δ) of the (002) to the (100) peak intensity, thereby confirming the effect of platelet orientation on $a_\perp$ [37,45].

4. Conclusions

In this work, we have demonstrated the facile and cost-effective preparation of low-density micro and nanoporous aramid films reinforced with hBN through the incorporation of hBN in the casting solution. When 10% hBN was used in the formulation following our preparation procedure, the dispersion of hBN platelets in the films was found to be homogeneous. This homogeneous distribution of hBN

contributed to the improvement of the mechanical performance of the aramid films. Specifically, μP-films containing 10% hBN exhibited a 130% increase in Young's modulus and a 68% reduction in density compared to commercially available unreinforced *m*-aramid films. This improvement can be attributed to the combined effect of the cellular structure and materials reinforcement. XRD analysis revealed that hBN platelets tend to increase their vertical orientation in the films when PVA is used as PP in the casting solution. The presence of hBN significantly enhanced the TC and TD of the films irrespective of their orientation. The out-of-plane TD exhibited an increase with an increase in the vertical orientation of the platelets. These results highlight the crucial role of porosity in modulating the anisotropic thermal conductive behavior of the film. Therefore, the ability to design reinforced porous aramids with different pores sizes, morphologies, and improved TD offers the possibility of developing tailored materials for specific applications. These advanced materials hold promise for various applications in the

aerospace industry, where there is a demand for thermally conductive high-performance composites with excellent mechanical properties and low density.

Funding

Author contributions statement

Andrea Rubio-Aguinaga: data collection and curation, investigation, validation, writing original draft. José Antonio Reglero-Ruiz: data collection and curation, investigationand methodology. Alejandra García-Gomez: conceptualization, supervision and validation. Elisa Peña Martín: formal análisis, methodology. Shinji Ando: formal análisis, supervision and validation. Asunción Muñoz: formal analysis, methodology, supervision. José Miguel García: conceptualization, project administration and visualization. Miriam Trigo-López: conceptualization, funding acquisition, investigation, visualization, project administration, validation and writing original draft. All authors reviewed the manuscript.

Declaration of competing interest

The authors declare that they have no known competing financial interests or personal relationships that could have appeared to influence the work reported in this paper.

Data availability

The raw/processed data required to reproduce these findings can be found at https://riubu.ubu.es/handle/10259/7628

Acknowledgments

Appendix A. Supplementary data

Supplementary data to this article can be found online at https://doi.org/10.1016/j.compscitech.2023.110211.

References

[1] M. Trigo-López, J.M. García, J.A.R. Ruiz, F.C. García, R. Ferrer, Aromatic polyamides, in: Encycl. Polym. Sci. Technol., John Wiley & Sons, Inc., Hoboken, NJ, USA, 2018, pp. 1–51, https://doi.org/10.1002/0471440264.pst249.pub2.

[2] A. Rubio-Aguinaga, J.A. Reglero-Ruiz, A. Muñoz, F.C. García, J.M. García, M. Trigo-López, Preparation of low-density high-performance porous aramid films using porosity promoter polymers, J. Appl. Polym. Sci. 139 (2022), https://doi.org/10.1002/app.53192.

[3] B.S. Pascual, M. Trigo-López, J.A. Reglero Ruiz, J.L. Pablos, J.C. Bertolín, C. Represa, J.V. Cuevas, F.C. García, J.M. García, Porous aromatic polyamides the easy and green way, Eur. Polym. J. 116 (2019) 91–98, https://doi.org/10.1016/j.eurpolymj.2019.03.058.

[4] S. Qingjin, H. Heji, L. Wei, L. Xiang, Aromatic Polyamide Porous Membrane, Method for Preparing, and Lithium Secondary Battery Having the Same, 2019. US 20190074500.

[5] M.H. Parekh, S. Oka, J. Lutkenhaus, V.G. Pol, Critical-point-dried, porous, and safer aramid nanofiber separator for high-performance durable lithium-ion batteries, ACS Appl. Mater. Interfaces 14 (2022) 29176–29187, https://doi.org/10.1021/acsami.2c04630.

[6] Z. Rafiee, S. Mallakpour, Synthesis and properties of novel brominated chiral polyamides derived from 5-[4-(2-tetrabromophthalimidylpropanoylamino)benzoylamino]isophthalic acid and aromatic diamines, Polym. Bull. 73 (2016) 1951–1964, https://doi.org/10.1007/s00289-015-1587-x.

[7] H.H. Hassan, A.F. Elhusseiny, Y.M. Elkony, E.-S.M. Mansour, Synthesis and characterization of thermally stable aromatic polyamides and poly(1,3,4-oxadiazole-amide)s nanoparticles containing pendant substituted bezamides, Chem. Cent. J. 7 (2013) 13, https://doi.org/10.1186/1752-153X-7-13.

[8] J. Zhao, H. Xu, X. Jiang, J. Yin, Multi-responsive wholly aromatic sulfonated polyamide ultra-sensitive to pH value, Sci. China Chem. 55 (2012) 2503–2506, https://doi.org/10.1007/s11426-012-4687-6.

[9] Y. Wang, T. Feng, J. Piao, J. Ren, M. Ou, Y. Wang, R. Lian, J. Cui, H. Guan, C. Jiao, X. Chen, Surface modification of epichlorohydrin-modified aramid nanofibers using ionic liquid to improve the fire safety and tensile strength of cotton fabrics, Polym. Adv. Technol. 33 (2022) 4302–4316, https://doi.org/10.1002/pat.5860.

[10] M. Trigo-López, S. Vallejos, J.A. Reglero Ruiz, A. García-Gómez, M. Seara-Martínez, F.C. García, J.M. García, High-performance nanoporous aramid films reinforced with functionalized carbon nanocharges using ionic liquids, Polymer (Guildf) 202 (2020), 122629, https://doi.org/10.1016/j.polymer.2020.122629.

[11] M. Trigo-López, A.M. Sanjuán, A. Mendía, A. Muñoz, F.C. García, J.M. García, Heteroaromatic polyamides with improved thermal and mechanical properties, Polymers 12 (2020) 1793, https://doi.org/10.3390/polym12081793.

[12] Y.J. Xu, Y. Ma, Y.C. Xie, Y. Zhou, H. Zhang, G.Y. Huang, Experimental and numerical study on the ballistic performance of a ZnO-modified aramid fabric, Int. J. Impact Eng. 175 (2023), 104519, https://doi.org/10.1016/j.ijimpeng.2023.104519.

[13] T. Ma, Y. Zhao, K. Ruan, X. Liu, J. Zhang, Y. Guo, X. Yang, J. Kong, J. Gu, Highly thermal conductivities, excellent mechanical robustness and flexibility, and outstanding thermal stabilities of aramid nanofiber composite papers with nacre-mimetic layered structures, ACS Appl. Mater. Interfaces 12 (2020) 1677–1686, https://doi.org/10.1021/acsami.9b19844.

[14] B.S. Pascual, M. Trigo-López, C. Ramos, M.T. Sanz, J.L. Pablos, F.C. García, J.A. Reglero Ruiz, J.M. García, Microcellular foamed aromatic polyamides (aramids). Structure, thermal and mechanical properties, Eur. Polym. J. 110 (2019) 9–13, https://doi.org/10.1016/j.eurpolymj.2018.11.007.

[15] A. Falin, Q. Cai, E.J.G. Santos, D. Scullion, D. Qian, R. Zhang, Z. Yang, S. Huang, K. Watanabe, T. Taniguchi, M.R. Barnett, Y. Chen, R.S. Ruoff, L.H. Li, Mechanical properties of atomically thin boron nitride and the role of interlayer interactions, Nat. Commun. 8 (2017), 15815, https://doi.org/10.1038/ncomms15815.

[16] A. Suhail, I. Lahiri, Two-dimensional hexagonal boron nitride and borophenes, in: Layer. 2D Adv. Mater. Their Allied Appl., Wiley, 2020, pp. 303–336, https://doi.org/10.1002/9781119655190.ch13.

[17] S. Roy, X. Zhang, A.B. Puthirath, A. Meiyazhagan, S. Bhattacharyya, M.M. Rahman, G. Babu, S. Susarla, S.K. Saju, M.K. Tran, L.M. Sassi, M.A.S.R. Saadi, J. Lai, O. Sahin, S.M. Sajadi, B. Dharmarajan, D. Salpekar, N. Chakingal, A. Baburaj, X. Shuai, A. Adumbumkulath, K.A. Miller, J.M. Gayle, A. Ajnsztajn, T. Prasankumar, V.V.J. Harikrishnan, V. Ojha, H. Kannan, A.Z. Khater, Z. Zhu, S. A. Iyengar, P.A. da S. Autreto, E.F. Oliveira, G. Gao, A.G. Birdwell, M.R. Neupane, T.G. Ivanov, J. Taha-Tijerina, R.M. Yadav, S. Arepalli, R. Vajtai, P.M. Ajayan, Structure, properties and applications of two-dimensional hexagonal boron nitride, Adv. Mater. 33 (2021), 2101589, https://doi.org/10.1002/adma.202101589.

[18] Z. Zhu, C. Li, E. Songfeng, L. Xie, R. Geng, C.-T. Lin, L. Li, Y. Yao, Enhanced thermal conductivity of polyurethane composites via engineering small/large sizes interconnected boron nitride nanosheets, Compos. Sci. Technol. 170 (2019) 93–100, https://doi.org/10.1016/j.compscitech.2018.11.035.

[19] L.-H. Zhao, L. Wang, Y.-F. Jin, J.-W. Ren, Z. Wang, L.-C. Jia, Simultaneously improved thermal conductivity and mechanical properties of boron nitride nanosheets/aramid nanofiber films by constructing multilayer gradient structure, Compos. Part B Eng. 229 (2022), 109454, https://doi.org/10.1016/j.compositesb.2021.109454.

[20] M. Li, Y. Zhu, C. Teng, Facial fabrication of aramid composite insulating paper with high strength and good thermal conductivity, Compos. Commun. 21 (2020), 100370, https://doi.org/10.1016/j.coco.2020.100370.

[21] M. Lin, Y. Li, K. Xu, Y. Ou, L. Su, X. Feng, J. Li, H. Qi, D. Liu, Thermally conductive nanostructured, aramid dielectric composite films with boron nitride nanosheets, Compos. Sci. Technol. 175 (2019) 85–91, https://doi.org/10.1016/j.compscitech.2019.02.006.

[22] G. Xiao, J. Di, H. Li, J. Wang, Highly thermally conductive, ductile biomimetic boron nitride/aramid nanofiber composite film, Compos. Sci. Technol. 189 (2020), 108021, https://doi.org/10.1016/j.compscitech.2020.108021.

[23] R. Mo, Z. Liu, W. Guo, X. Wu, Q. Xu, Y. Min, J. Fan, J. Yu, Interfacial crosslinking for highly thermally conductive and mechanically strong boron nitride/aramid nanofiber composite film, Compos. Commun. 28 (2021), 100962, https://doi.org/10.1016/j.coco.2021.100962.

[24] H. Ding, S.N. Leung, Modelling of effective thermal conductivity of polymer matrix composite foams with biaxially aligned filler networks, J. Cell. Plast. 52 (2016) 89–106, https://doi.org/10.1177/0021955X14566211.

[25] M. Hamidinejad, A. Zandieh, J.H. Lee, J. Papillon, B. Zhao, N. Moghimian, E. Maire, T. Filleter, C.B. Park, Insight into the directional thermal transport of hexagonal boron nitride composites, ACS Appl. Mater. Interfaces 11 (2019) 41726–41735, https://doi.org/10.1021/acsami.9b16070.

[26] B. Ghosh, F. Xu, D.M. Grant, P. Giangrande, C. Gerada, M.W. George, X. Hou, Highly ordered BN ⊥ –BN ⊥ stacking structure for improved thermally conductive polymer composites, Adv. Electron. Mater. 6 (2020), 2000627, https://doi.org/10.1002/aelm.202000627.

[27] R.Y. Tay, H. Li, J. Lin, H. Wang, J.S.K. Lim, S. Chen, W.L. Leong, S.H. Tsang, E.H. T. Teo, Lightweight, superelastic boron nitride/polydimethylsiloxone foam as air dielectric substitute for multifunctional capacitive sensor applications, Adv. Funct. Mater. 30 (2020), 1909604, https://doi.org/10.1002/adfm.201909604.

[28] A.C.M. de Moraes, W.J. Hyun, N.S. Luu, J.-M. Lim, K.-Y. Park, M.C. Hersam, Phase-inversion polymer composite separators based on hexagonal boron nitride nanosheets for high-temperature lithium-ion batteries, ACS Appl. Mater. Interfaces 12 (2020) 8107–8114, https://doi.org/10.1021/acsami.9b18134.

[29] K. Yang, Y.Y. Kang, H.J. Ahn, D.-G. Kim, N.K. Park, S.Q. Choi, J.C. Won, Y.H. Kim, Porous boron nitride/polyimide composite films with high thermal diffusivity and low dielectric properties via high internal phase Pickering emulsion method, J. Ind. Eng. Chem. 82 (2020) 173–179, https://doi.org/10.1016/j.jiec.2019.10.010.

[30] H.-J. Pi, X.-X. Liu, J.-Y. Liao, Y.-Y. Zhou, C. Meng, Lightweight polyethylene/hexagonal boron nitride hybrid thermal conductor fabricated by melt compounding plus salt leaching, Polymers 14 (2022) 852, https://doi.org/10.3390/polym14050852.

[31] W. Wu, M. Zheng, K. Lu, F. Liu, Y.-H. Song, M. Liu, Z.-M. Dang, Thermally conductive composites based on hexagonal boron nitride nanosheets for thermal management: fundamentals to applications, Compos. Part A Appl. Sci. Manuf. 169 (2023), 107533, https://doi.org/10.1016/j.compositesa.2023.107533.

[32] ASTM-D5930-17, Standard Test Method for Thermal Conductivity of Plastics by Means of a Transient Line-Source Technique, 2017.

[33] E. Gariboldi, L.P.M. Colombo, D. Fagiani, Z. Li, Methods to characterize effective thermal conductivity, diffusivity and thermal response in different classes of composite phase change materials, Materials (Basel) 12 (2019) 2552, https://doi.org/10.3390/ma12162552.

[34] T. Hashimoto, J. Morikawa, T. Kurihara, T. Tsuji, Frequency dependent thermal diffusivity of polymers by temperature wave analysis, Thermochim. Acta 304–305 (1997) 151–156, https://doi.org/10.1016/S0040-6031(97)00026-9.

[35] Z. Wang, T. Zhang, J. Wang, G. Yang, M. Li, G. Wu, The investigation of the effect of filler sizes in 3D-BN skeletons on thermal conductivity of epoxy-based composites, Nanomaterials 12 (2022) 446, https://doi.org/10.3390/nano12030446.

[36] F. Guo, J. Zhao, F. Li, D. Kong, H. Guo, X. Wang, H. Hu, L. Zong, J. Xu, Polar crystalline phases of PVDF induced by interaction with functionalized boron nitride nanosheets, CrystEngComm 22 (2020) 6207–6215, https://doi.org/10.1039/D0CE01001D.

[37] M. Tanimoto, T. Yamagata, K. Miyata, S. Ando, Anisotropic thermal diffusivity of hexagonal boron nitride-filled polyimide films: effects of filler particle size, aggregation, orientation, and polymer chain rigidity, ACS Appl. Mater. Interfaces 5 (2013) 4374–4382, https://doi.org/10.1021/am400615z.

[38] J. Liu, W. Li, Y. Guo, H. Zhang, Z. Zhang, Improved thermal conductivity of thermoplastic polyurethane via aligned boron nitride platelets assisted by 3D printing, Compos. Part A Appl. Sci. Manuf. 120 (2019) 140–146, https://doi.org/10.1016/j.compositesa.2019.02.026.

[39] H.-J. Pi, X.-X. Liu, J.-Y. Liao, Y.-Y. Zhou, C. Meng, Lightweight polyethylene/hexagonal boron nitride hybrid thermal conductor fabricated by melt compounding plus salt leaching, Polymers 14 (2022) 852, https://doi.org/10.3390/polym14050852.

[40] C. Pan, K. Kou, Y. Zhang, Z. Li, G. Wu, Enhanced through-plane thermal conductivity of PTFE composites with hybrid fillers of hexagonal boron nitride platelets and aluminum nitride particles, Compos. Part B Eng. 153 (2018) 1–8, https://doi.org/10.1016/j.compositesb.2018.07.019.

[41] S. Rouhi, Molecular dynamics simulation of the adsorption of polymer chains on CNTs, BNNTs and GaNNTs, Fibers Polym. 17 (2016) 333–342, https://doi.org/10.1007/s12221-016-5676-8.

[42] J. Zhang, C. Li, C. Yu, X. Wang, Q. Li, H. Lu, Q. Zhang, J. Zhao, E. Songfeng, M. Hu, Y. Yao, Large improvement of thermal transport and mechanical performance of polyvinyl alcohol composites based on interface enhanced by SiO2 nanoparticle-modified-hexagonal boron nitride, Compos. Sci. Technol. 169 (2019) 167–175, https://doi.org/10.1016/j.compscitech.2018.11.001.

[43] B. Notario, J. Pinto, E. Solorzano, J.A. de Saja, M. Dumon, M.A. Rodríguez-Pérez, Experimental validation of the Knudsen effect in nanocellular polymeric foams, Polymer (Guildf) 56 (2015) 57–67, https://doi.org/10.1016/j.polymer.2014.10.006.

[44] I. Sánchez-Calderón, V. Bernardo, J. Martín-de-León, M.Á. Rodríguez-Pérez, Thermal conductivity of low-density micro-and nanocellular poly(methyl-methacrylate) (PMMA): experimental and modeling, Mater. Des. 221 (2022), 110938, https://doi.org/10.1016/j.matdes.2022.110938.

[45] M. Tanimoto, S. Ando, Prevention of void formation in particulate-filled polymer composites: effects of thermoplastic matrices and residual solvent, Compos. Sci. Technol. 123 (2016) 268–275, https://doi.org/10.1016/j.compscitech.2015.12.022.